Supplementary Information

Dual interphase design stabilized Mg-metal batteries

Wenwen Wang[1,#], Chengyi Zhang[2,#], Xinquan Ma[1,#], Weixiao Wang[1,#], Qin Su[1], Juncai Long[3], Dongyao Zhu[1], Jinghao Li[1], Ao Xu[1], Rui Fang[4], Yuhang Dai[5,*], Guanbin Gao[1,*], Qinyou An[1,*]

[1]State Key Laboratory of Advanced Technology for Materials Synthesis and Processing, Wuhan University of Technology, Wuhan 430070, PR China.

[2]School of Chemical Sciences, The University of Auckland, Auckland 1010, New Zealand.

[3]Department of Industrial and Systems Engineering, The Hong Kong Polytechnic University, Hung Hom, Hong Kong 999077, PR China.

[4]Department of Chemical and Environmental Engineering, University of Cincinnati, Cincinnati, OH 45220, USA.

[5]Institute for Integrated Cell-Material Sciences, Kyoto University, Yoshida, Sakyo-ku, Kyoto 606-8501, Japan.

[#]These authors contributed equally: Wenwen Wang, Chengyi Zhang, Xinquan Ma, and Weixiao Wang

[*]Corresponding emails: dai.yuhang.72z@st.kyoto-u.ac.jp (Y.D.); gbgao@whut.edu.cn (G.G.); anqinyou86@whut.edu.cn (Q.A.);

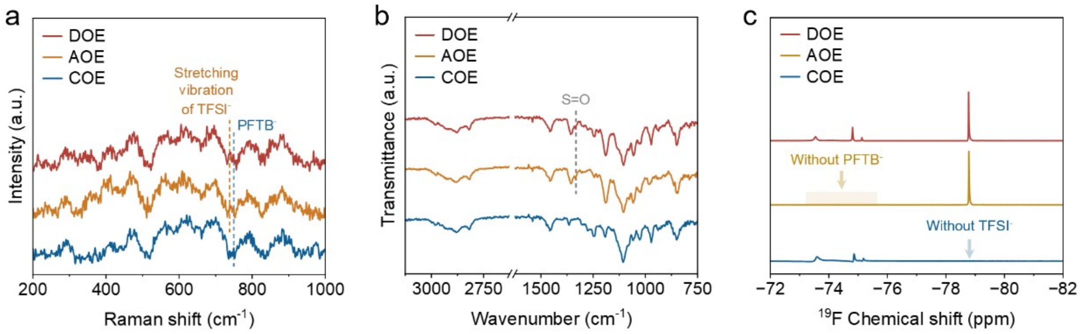

Figure S1. Spectroscopic characterization of DOE, AOE, and COE electrolytes (a-c) (a) Raman spectra, (b) FTIR spectra, and (c) Solution ^{19}NMR spectra of DOE, AOE, and COE.

Raman spectra (Figure S1a) show the characteristic bands of TFSI$^-$ in DOE and AOE, while these features are absent in COE[1,2]. FTIR spectra (Figure S1b) similarly display N-S stretching from TFSI$^-$ in DOE and AOE only[3].

In the ^{19}F NMR spectra (Figure S1c), the signals from PFTB$^-$ are observed in DOE and COE but not in AOE[4], whereas TFSI$^-$ resonances appear in DOE and AOE but not in COE[5,6]. These results confirm the intended compositions of the three electrolytes.

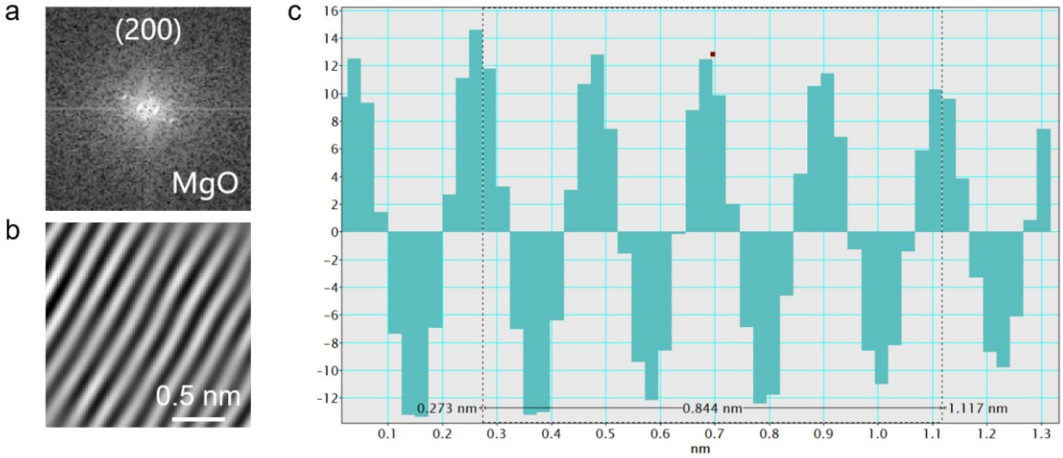

Figure S2. Identification of MgO crystallites in the CEI of the COE cathode.
(a-b) (a) Fast Fourier transform (FFT) patterns and (b) corresponding inverse FFT images collected from partially crystalline regions of the CEI.
(c) Line profile of the lattice fringes used to determine the interplanar spacing.

The measured d-spacing matches well with the (200) plane of MgO[7], confirming the presence of MgO crystallites in the CEI formed in the COE electrolyte.

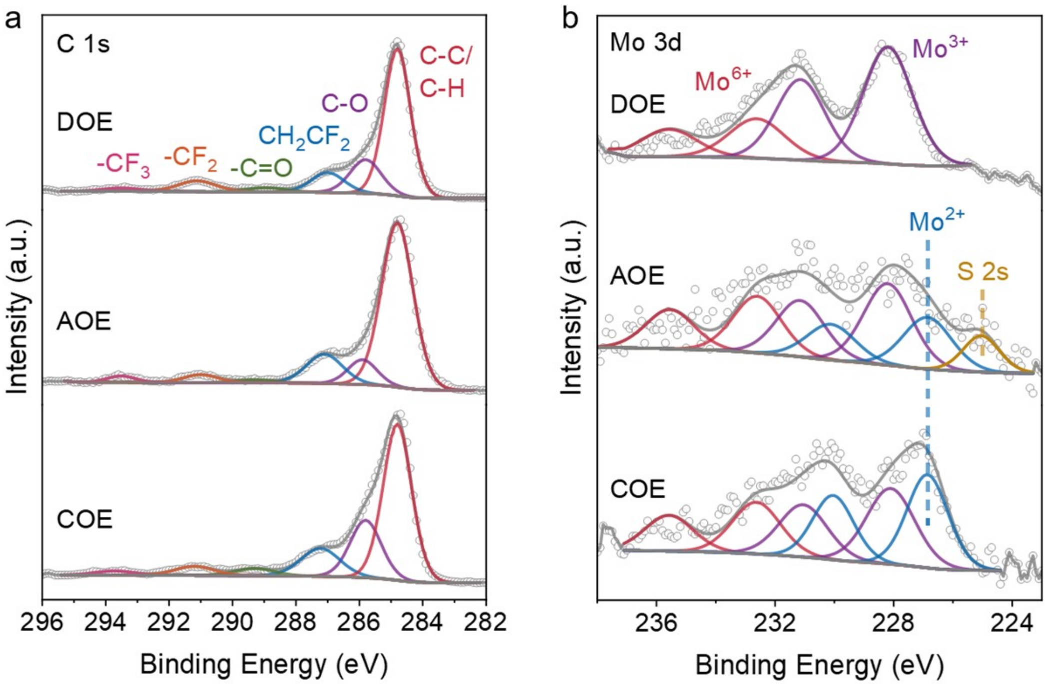

Figure S3. XPS signatures of cathode-anode cross-talk after 20 cycles.
(a-b) XPS spectra collected after 20 cycles, showing (a) C 1s from Mo_6S_8 cathodes and (b) Mo 3d from the Mg-anode.

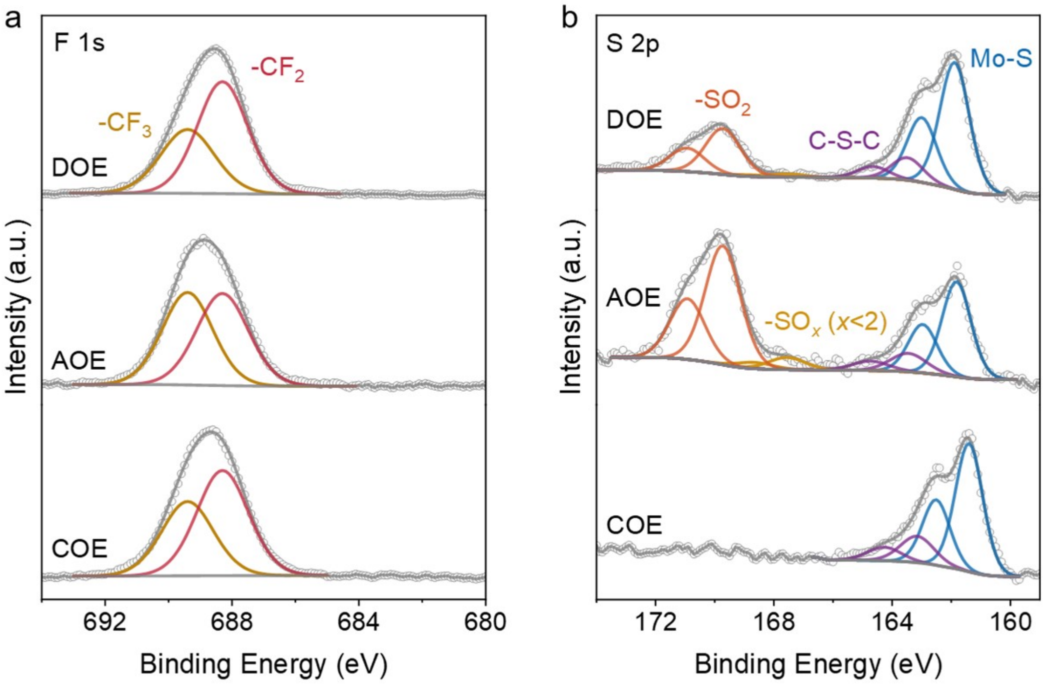

Figure S4. XPS results of CEIs formed in DOE, AOE, and COE electrolytes. (a-b) XPS spectra of (a) F 1s, (b) S 2p obtained from the Mo_6S_8 cathode surfaces after 20 cycles in the three electrolytes.

XPS reveals pronounced electrolyte-dependent CEI chemistries. In the F 1s region, CF_2-related features appear in all samples (Figure S4a), which are primarily associated with the PVDF binder. Notably, DOE and COE exhibit an enhanced CF_2 contribution relative to AOE, consistent with preferential oxidative decomposition of the $PFTB^-$ anion at the cathode surface. In the S 2p region, SO_x-containing species are detected for DOE and AOE (Figure S4b)[8,9], consistent with $TFSI^-$-derived decomposition products.

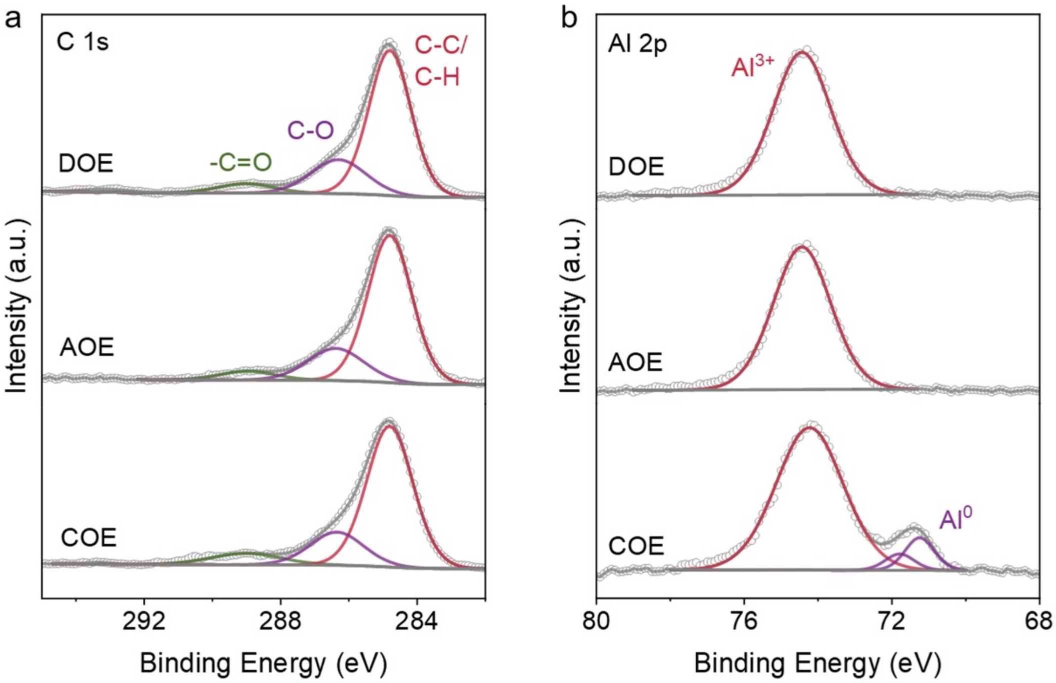

Figure S5. XPS spectra of SEIs on Mg anodes after 20 cycles in DOE, AOE, and COE electrolytes, revealing parasitic interfacial chemistry.
(a-b) (a) C 1s and (b) Al 2p spectra of SEIs formed in the three electrolytes.

XPS analysis of the cycled Mg anodes reveals clear differences in SEI composition among the electrolytes. After charge calibration using the C 1s signal (Figure S5a)[10,11], the Al 2p spectra show that DOE and AOE are dominated by Al^{3+} species, whereas an additional Al^{0} component is observed exclusively for COE. This result suggests that, compared with the TFSI^{-}-containing DOE and AOE electrolytes, COE fails to establish a sufficiently passivating interphase on the Mg anode, thereby allowing parasitic reduction of $AlCl_3$-derived species and Al co-deposition.

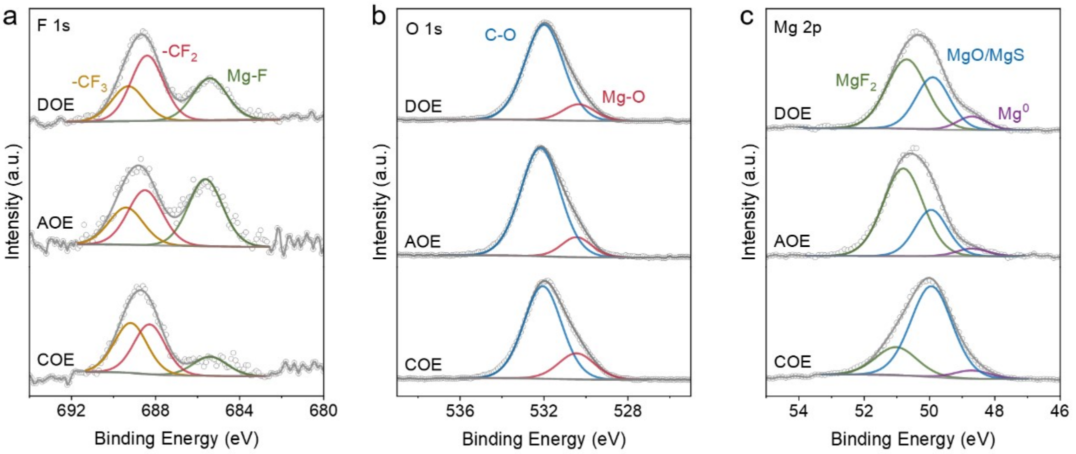

Figure S6. XPS spectra of SEIs on Mg anodes after 20 cycles in DOE, AOE, and COE electrolytes, revealing distinct interphase composition.
(a-c) (a) F 1s, (b) O 1s, and (c) Mg 2p spectra of SEIs formed in the three electrolytes, respectively.

The composition of the Mg interphase differs markedly across electrolytes. DOE and AOE exhibit pronounced Mg-F contributions in both the F 1s and Mg 2p regions (Figure S6a, c), supporting the formation of MgF_2-rich SEIs in the presence of $TFSI^-$. In contrast, COE shows an enhanced MgO contribution in the Mg 2p and O 1s spectra (Figure S6b, c)[12], indicating a MgO-dominated interphase.

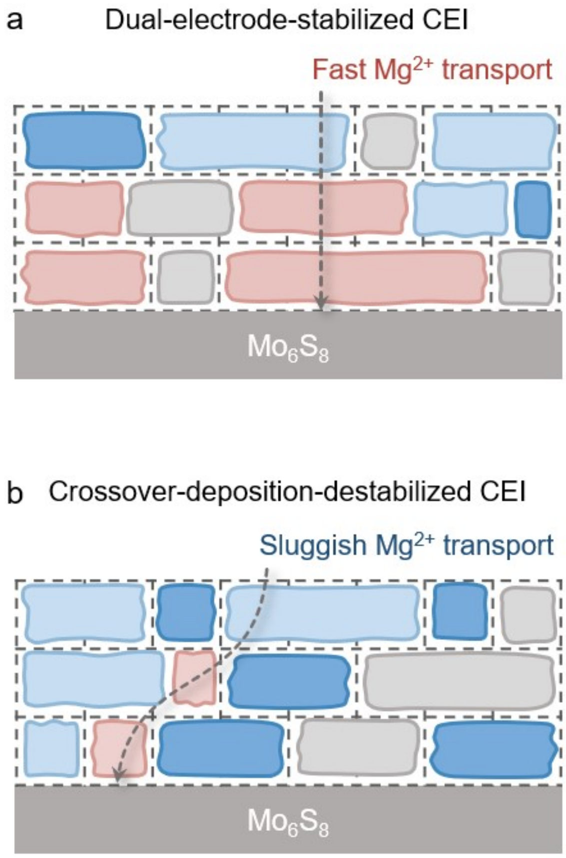

Figure S7. Semi-quantitative CEI depth profiling by XPS.

(a-b) Depth-dependent proportions of CEI components derived from XPS depth profiling for cathodes cycled in (a) DOE and (b) COE.

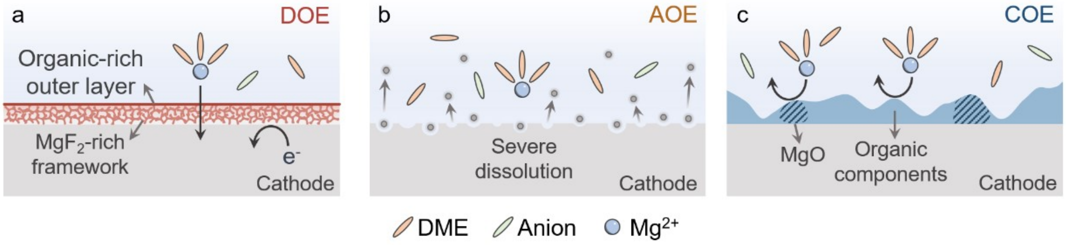

Figure S8. Schematic summary of electrolyte-derived CEI structures.
(a-c) Schematic illustrations of cathode interphases formed in (a) DOE, (b) AOE, and (c) COE electrolytes.

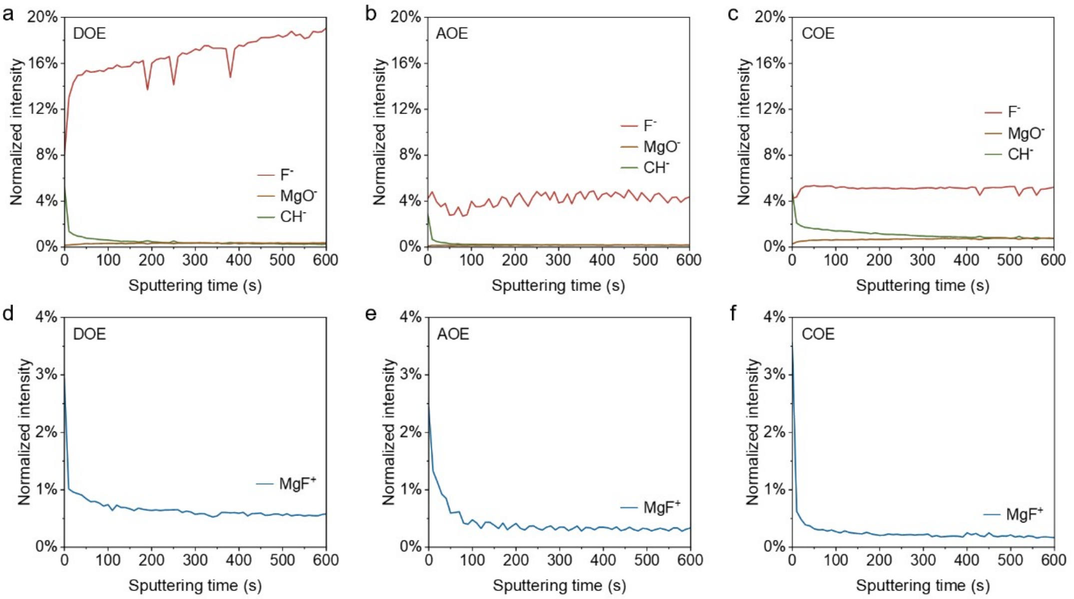

Figure S9. TOF-SIMS depth profiles of SEIs formed on Mg anodes in DOE, AOE, and COE electrolytes.

(a-c) Normalized negative-ion depth profiles (F^-, MgO^-, and CH^-) for DOE, AOE, and COE, respectively.

(d-f) Normalized positive-ion depth profiles (MgF^+) for DOE, AOE, and COE, respectively.

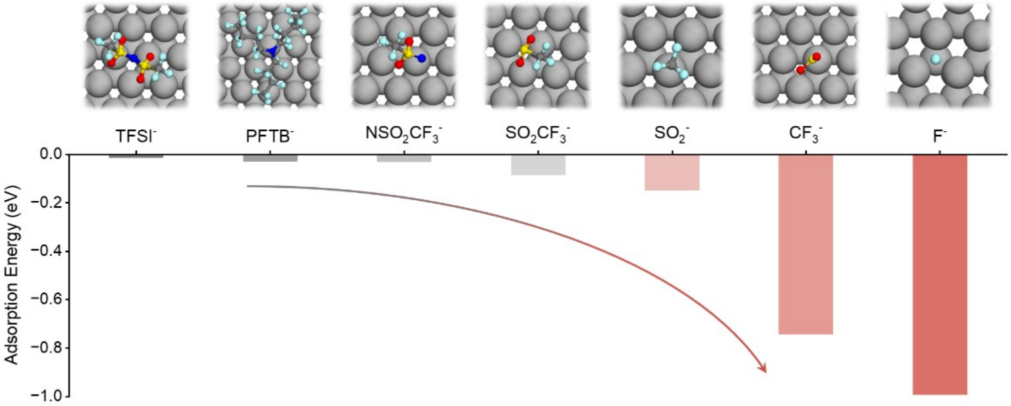

Figure S10. Preferential adsorption of fluorinated fragments on Mg metal. Calculated adsorption energies (Eads) of key anionic fragments derived from Mg(TFSI)$_2$ and Mg(PFTB)$_2$ on the Mg metal surface.

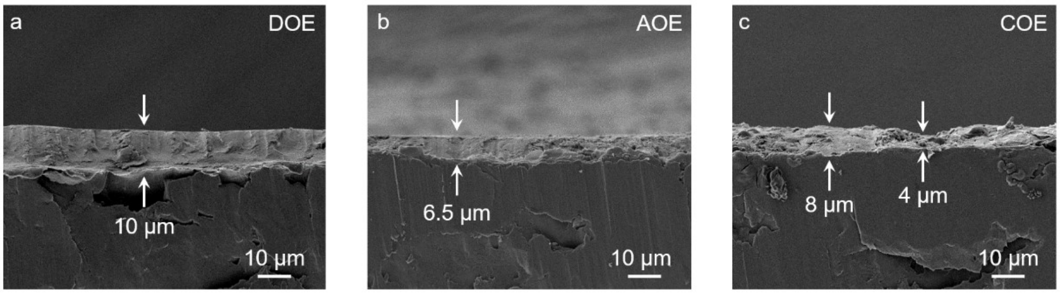

Figure S11. Electrolyte-dependent morphology of Mg deposits after 200 cycles. (a-c) Cross-sectional SEM images of Mg anodes harvested from Mg||Mo_6S_8 cells after 200 cycles (fully charged state) in (a) DOE, (b) AOE, and (c) COE electrolytes.

Cross-sectional imaging of Mg anodes harvested after 200 cycles at the fully charged state shows that DOE produces a thicker and more compact Mg deposit, consistent with higher reversible capacity and more stable Mg plating and stripping. AOE yields a thinner and more porous yet comparatively uniform layer, while COE results in the thinnest and most heterogeneous deposition.

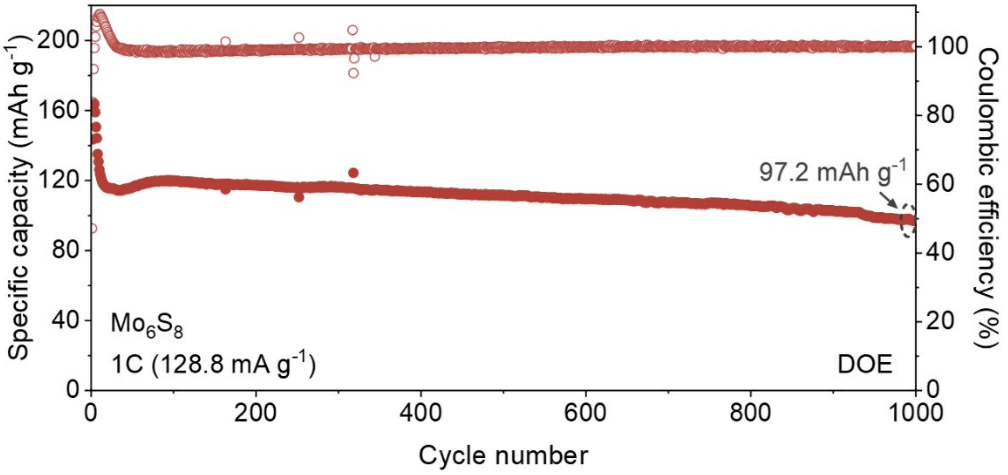

Figure S12. Long-term cycling stability enabled by the DOE electrolyte. Cycling performance of Mo_6S_8 cathodes at 1 C in DOE.

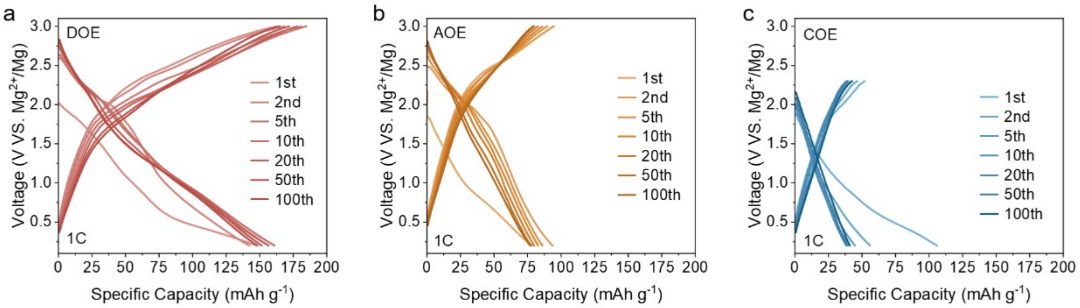

Figure S13. Galvanostatic profiles of Mg||PANI cells at 1C in different electrolytes. (a-c) Selected charge/discharge curves (1st, 2nd, 5th, 10th, 20th, 50th, and 100th cycles) of Mg||PANI cells operated at 1C in (a) DOE, (b) AOE, and (c) COE.

DOE delivers the highest specific capacity with the most stable voltage profiles upon cycling. In contrast, AOE exhibits progressive capacity decay, and COE maintains consistently lower capacities throughout cycling.

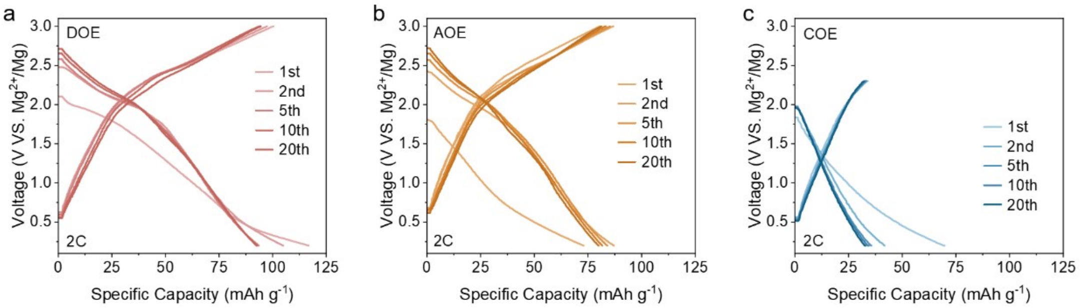

Figure S14. Galvanostatic profiles of Mg||PANI cells at 2C in different electrolytes. (a-c) Selected charge/discharge profiles (1st, 2nd, 5th, 10th, and 20th cycles) of Mg||PANI cells operated at 2C in (a) DOE, (b) AOE, and (c) COE.

At 2C, DOE delivers the highest specific capacity and retains a well-defined, stable discharge plateau with relatively small voltage hysteresis over repeated cycling. By contrast, AOE shows progressive polarization growth accompanied by gradual attenuation of the discharge plateau. COE exhibits the lowest capacity and the largest polarization throughout.

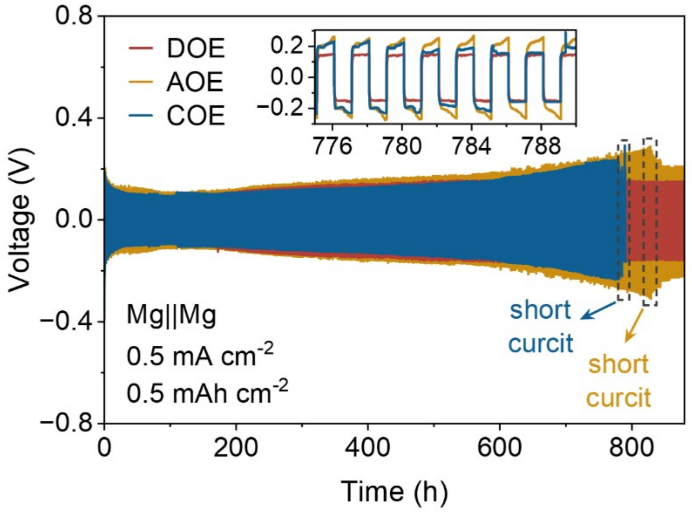

Figure S15. Long-term Mg plating/stripping stability in Mg||Mg symmetric cells. Galvanostatic voltage profiles of Mg||Mg symmetric cells cycled in DOE, AOE, and COE at 0.5 mA cm^{-2} with an areal capacity of 0.5 mAh cm^{-2}.

Galvanostatic cycling of Mg||Mg symmetric cells at 0.5 mA cm^{-2} (0.5 mAh cm^{-2}) reveals clear electrolyte-dependent interfacial stability. DOE sustains a lower and more stable polarization over prolonged cycling. In contrast, AOE and COE exhibit progressively increasing overpotential and fail by short circuit at ~830 h and ~780 h, respectively, indicating inferior interphase robustness under extended Mg plating/stripping.

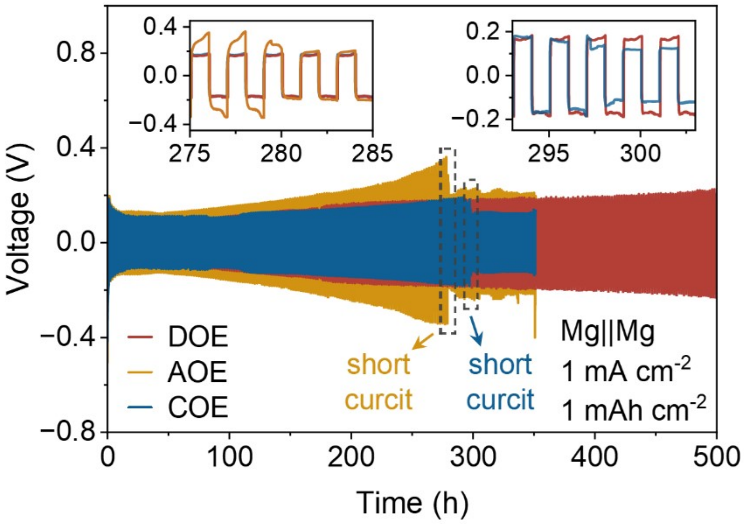

Figure S16. High-throughput Mg plating/stripping stability in Mg||Mg cells. Long-term stability of Mg plating/stripping at 1 mA cm^{-2} with an areal capacity of 1 mAh cm^{-2}.

Under a more stringent condition of 1 mA cm^{-2} with an areal capacity of 1 mAh cm^{-2}, DOE sustains stable Mg plating/stripping for 500 h with a low, steady overpotential. In contrast, AOE and COE exhibit progressively increasing polarization and fail by short circuit at ~280 h and ~300 h, respectively, indicating inferior interphase stability under high-throughput cycling.

The DOE performance in symmetric cells is comparable but more stable, while emphasizing that the more significant benefit of DOE is reflected in the full-cell configuration, where both anodic and cathodic interfacial stability play important roles.

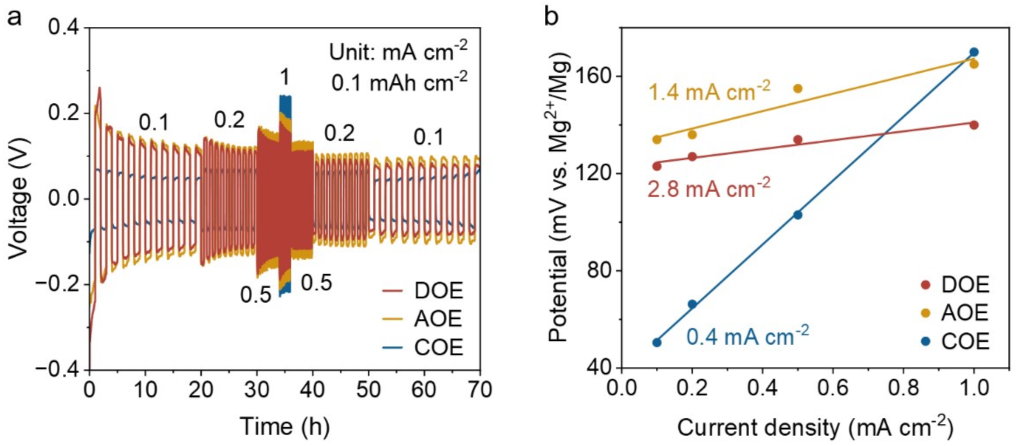

Figure S17. Mg||Mg interfacial kinetics.

(a) Rate performance of Mg||Mg symmetric cells at a fixed areal capacity of 0.1 mAh cm^{-2}.

(b) Exchange current densities (i_0) extracted from polarization curves measured at different scan rates.

Rate tests at a fixed areal capacity of 0.1 mAh cm^{-2} show that DOE maintains more stable polarization across current densities from 0.1 to 1 mA cm^{-2} (Figure S17a). Consistently, kinetic analysis yields the highest exchange current density for DOE (i_0 = 2.8 mA cm^{-2}), followed by AOE (1.4 mA cm^{-2}) and COE (0.4 mA cm^{-2}) (Figure S17b), indicating accelerated interfacial charge-transfer kinetics in DOE[13].

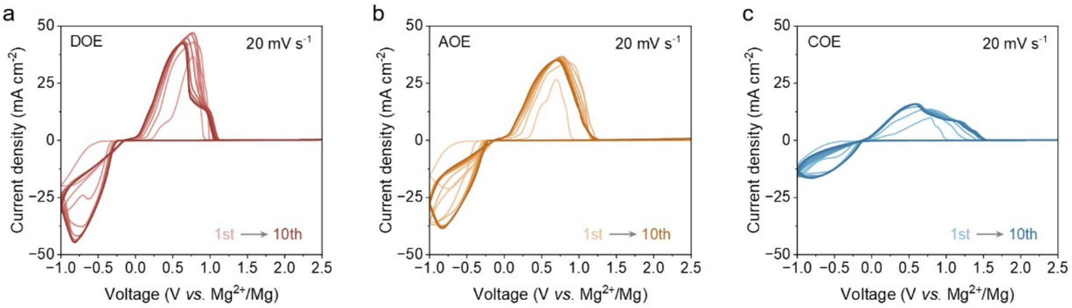

Figure S18. Cyclic voltammetry (CV) of Mg plating/stripping in Mg||Mo cells. (a-c) CV curves collected in (a) DOE, (b) AOE, and (c) COE at 20 mV s^{-1}, showing the first 10 cycles.

CV was performed in Mg||Mo asymmetric cells to probe Mg plating/stripping kinetics. At the same scan rate, DOE delivers higher and sharper plating/stripping peaks with a smaller peak-to-peak separation than AOE and COE, indicating reduced interfacial polarization and faster kinetics. AOE exhibits an intermediate response. In contrast, COE shows markedly broadened peaks with strongly suppressed currents, consistent with sluggish Mg plating/stripping and elevated interfacial resistance.

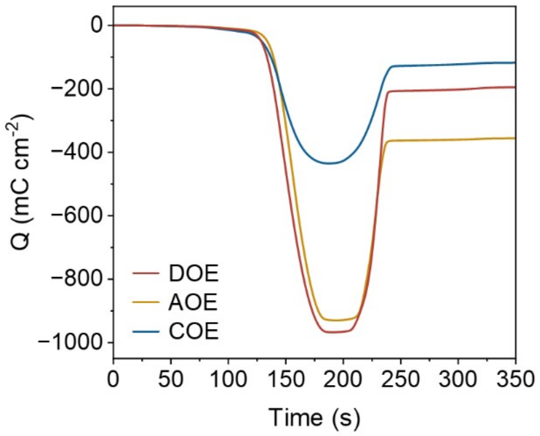

Figure S19. Charge-time (Q-t) characteristics of Mg plating/stripping in Mg||Mo cells.

Q-t profiles extracted from the first-cycle cyclic voltammetry of Mg||Mo cells in DOE, AOE, and COE electrolytes at 20 mV s^{-1}.

Integrating the first-cycle CV yields Q-t profiles[14]. DOE and AOE show a larger plating charge magnitude than COE, indicating higher Mg deposition charge throughput. During stripping, DOE exhibits a smaller residual Q than AOE, suggesting improved reversibility at comparable deposited charge. In contrast, COE delivers a much lower charge throughput despite a small residual Q, consistent with strongly limited Mg deposition/stripping.

Supplementary Note 1. Rationale for the voltage-window selection for COE.

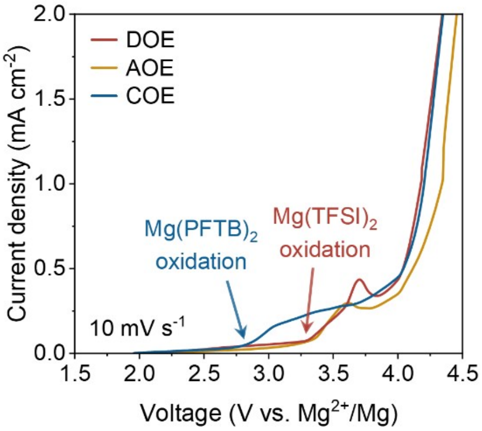

Figure S20. Oxidative stability of electrolytes in Mg||Mo cells.
LSV curves showing the oxidation stability of the three electrolytes in Mg||Mo cells.

To enable a fair electrochemical comparison while minimizing artefacts from electrolyte oxidation, the operating voltage window of COE was optimized for each cathode chemistry. This need is supported by linear sweep voltammetry (LSV) in Mg||Mo cells, where COE shows an earlier onset of anodic current at ~2.8 V, whereas DOE and AOE maintain near-baseline currents up to ~3.3 V (Figure S20), indicating a narrower oxidative stability margin for COE.

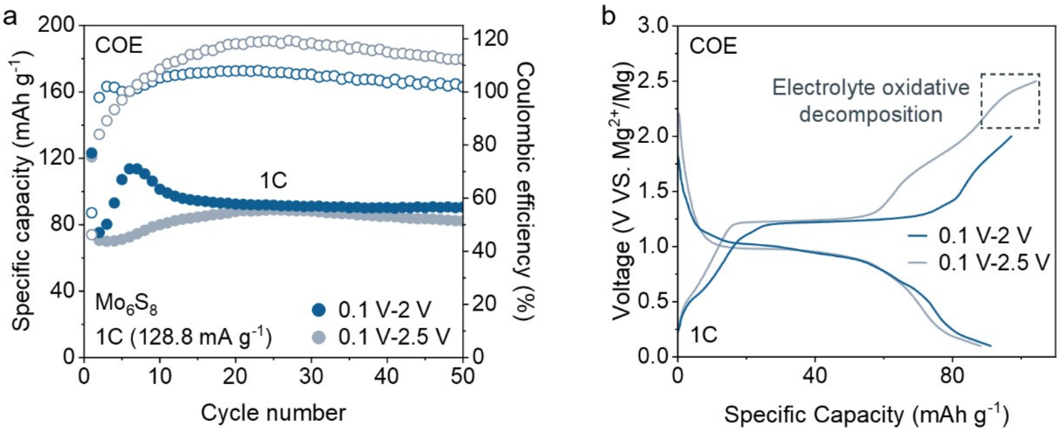

Figure S21. Influence of voltage window on the cycling performance of Mg||Mo$_6$S$_8$ cells in the COE electrolyte.
(a) Cycling performance of Mg||Mo$_6$S$_8$ cells using the COE electrolyte in the voltage windows of 0.1-2.0 V and 0.1-2.5 V.
(b) Corresponding galvanostatic charge-discharge (GCD) profiles at the 30th cycle for the two voltage windows.

Consistent with the LSV trend, in Mg||Mo$_6$S$_8$ cells, extending the upper cutoff to 2.5 V leads to markedly reduced and unstable coulombic efficiency together with lower discharge capacities and pronounced overcharge features in the charge profile (Figure

S21), indicative of oxidative degradation in COE on Mo_6S_8. Restricting the window to 0.1-2.0 V effectively suppresses these parasitic processes, resulting in reduced polarization and improved cycling stability. Therefore, 0.1-2.0 V is adopted as the optimized range for the electrochemical comparison of COE in the main text.

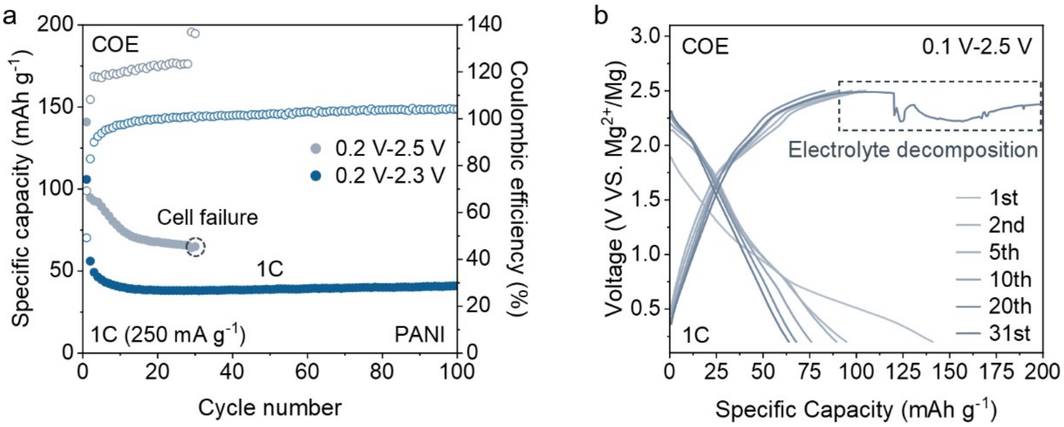

Figure S22. Effect of voltage window on the cycling stability of Mg||PANI cells in the COE electrolyte.

(a) Cycling performance of Mg||PANI cells at 1 C in the COE electrolyte using voltage windows of 0.1-2.3 V and 0.1-2.5 V.

(b) Corresponding GCD profiles at selected cycles (1st, 2nd, 5th, 10th, 20th, and 31st) for the two voltage windows.

A similar voltage-window dependence is observed for Mg||PANI cells. At an extended window of 0.1-2.5 V, the COE-based Mg||PANI cell shows a higher initial discharge capacity but undergoes rapid performance decay and failure within ~30 cycles, accompanied by strong overcharge signatures in the charge curves (Figure S22). In contrast, limiting the upper cutoff to 2.3 V effectively suppresses such overcharge signatures and enhances cycling stability. Accordingly, 0.1-2.3 V is adopted for COE in the main-text comparison.

Supplementary Note 2. Decoupling Cl-related contributions to the interphase.

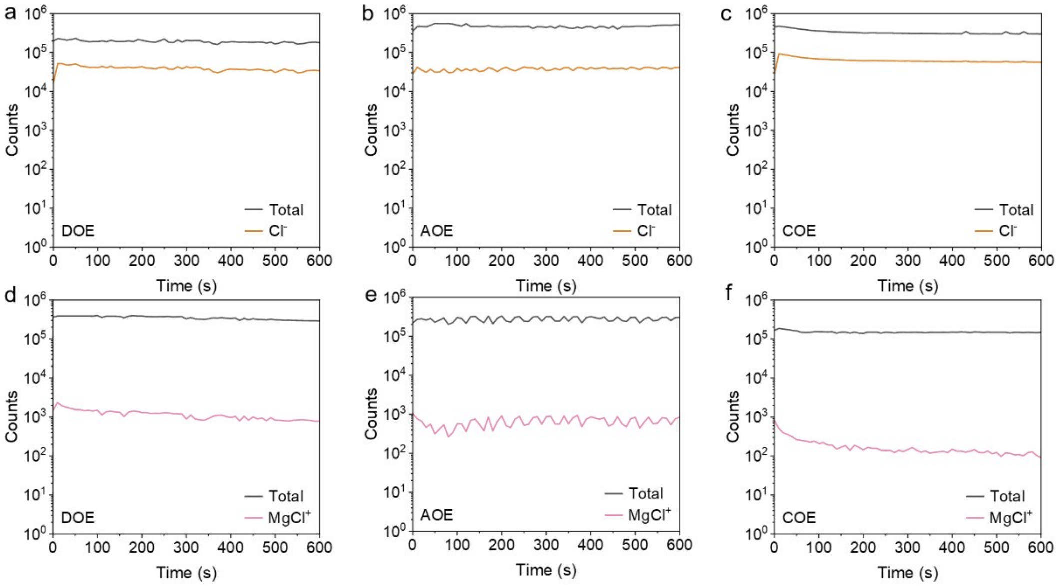

Figure S23. TOF-SIMS depth profiles of SEIs formed on Mg anodes in DOE, AOE, and COE electrolytes.

(a-c) Normalized negative-ion depth profiles (Cl^-) for DOE, AOE, and COE, respectively.

(d-f) Normalized positive-ion depth profiles ($MgCl^+$) for DOE, AOE, and COE, respectively.

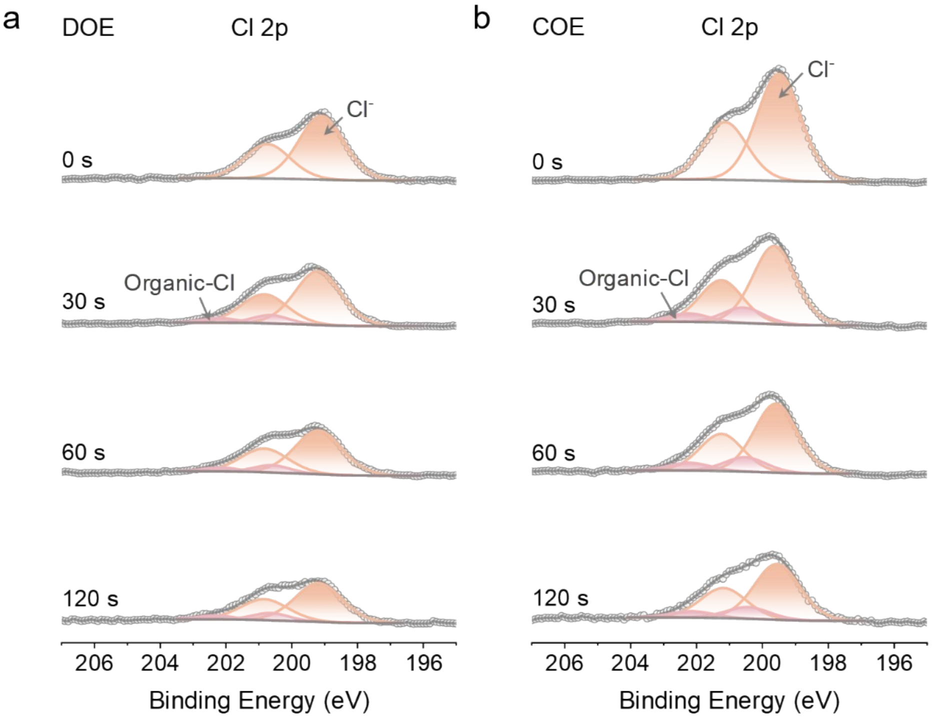

Figure S24. XPS depth profiling of the Cl 2p on Mo_6S_8 cathodes cycled in (a) DOE and (b) COE for 20 cycles.

These results indicate that Cl-related species are indeed incorporated into the interphases and constitute a common chemical background in all MACC-based electrolytes. They also suggest that Cl-related participation is somewhat more pronounced in COE, as reflected by the higher Cl^- signal in the SEI (Figure S23) and the consistently stronger Cl 2p signal in the CEI depth profiles (Figure S24). Nevertheless, these differences remain relatively modest and are not accompanied by substantial $MgCl^+$ enrichment in the SEI or obvious Cl-containing components in the CEI. Cl-related chemistry is therefore unlikely to account for the major electrolyte-dependent differences in interphase composition and electrochemical behavior. Instead, these differences are primarily governed by the additive-derived chemistries of $TFSI^-$ and $PFTB^-$, while Cl-related species remain a common contributing component across all MACC-based electrolytes.

Supplementary Note 3. Selective decomposition of TFSI⁻ and PFTB⁻.

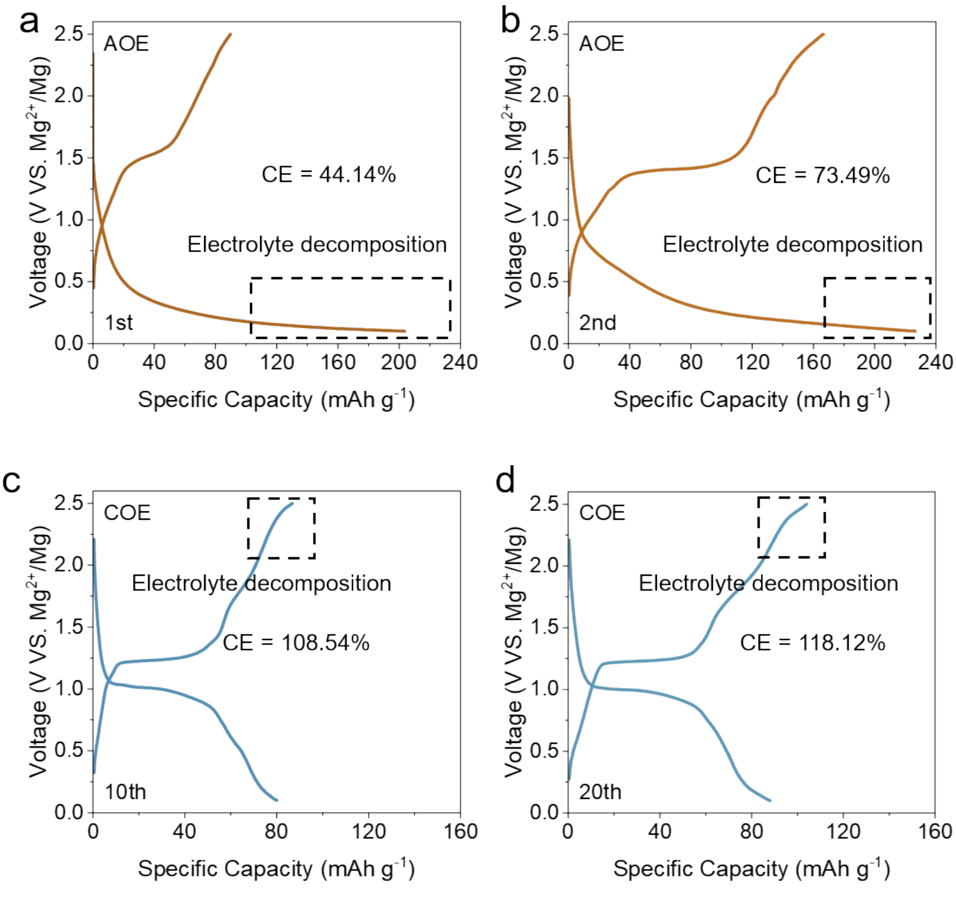

Figure S25. (a, b) Selected GCD curves (1st, 2nd) of Mg||Mo_6S_8 cells operated at 1C in AOE. (c, d) Selected GCD curves (10th, 20th) of Mg||Mo_6S_8 cells operated at 1C in COE.

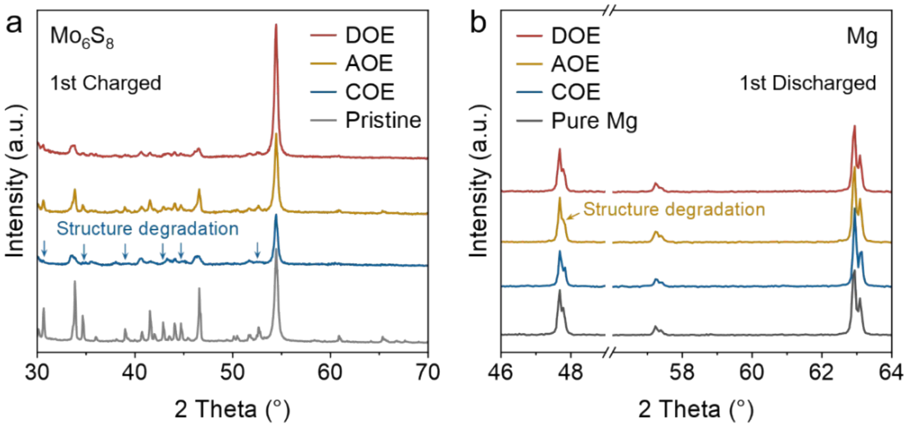

Figure S26. Structural stability of Mo_6S_8 cathodes and Mg anodes in different electrolytes.

(a) XRD patterns of Mo_6S_8 cathodes after the first charge in DOE, AOE, and COE electrolytes, together with the pristine Mo_6S_8 reference.

(b) XRD patterns of Mg anodes after the first discharge in the corresponding electrolytes, accompanied by the pristine Mg reference.

To provide additional mechanistic support, we further analyzed the electrochemical signatures of the three electrolytes. In AOE, the first two discharge curves exhibit a pronounced long tail at low potential (Figure S25a, b). This feature indicates an additional low-potential reductive process during the initial discharge, consistent with preferential reductive decomposition of $TFSI^-$ at the anode and concomitant SEI formation. Consistent with this interpretation, the Mg electrode in AOE shows noticeable degradation of its XRD peaks after the first discharge process, suggesting early-stage anode-side interfacial degradation (Figure S26b). In contrast, for COE, when the upper cutoff voltage was extended from 2.0 V to 2.5 V, clear additional high-voltage charging features emerged at the 10th and 20th cycles (Figure S25c, d). This behavior suggests the occurrence of parasitic oxidation at elevated potentials, consistent with $PFTB^-$ involved CEI formation at the cathode. Correspondingly, the Mo_6S_8 cathode in COE exhibits degradation of its XRD peaks after the first cycle, further supporting cathode-side interfacial degradation (Figure S26a).

Thus, the dual-interphase architecture in DOE is established in a spatiotemporally differentiated manner: SEI formation is initiated first at the Mg anode during the initial discharge, whereas CEI formation is triggered subsequently at the cathode as the cell enters the oxidative regime upon charging.

Supplementary Note 4. Properties of the MgF_2-containing interphase.

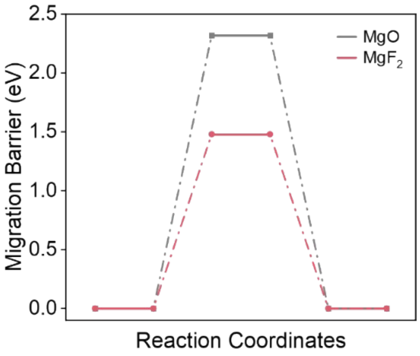

Figure S27. Mg^{2+} migration barriers of MgO and MgF_2 from DFT calculations.

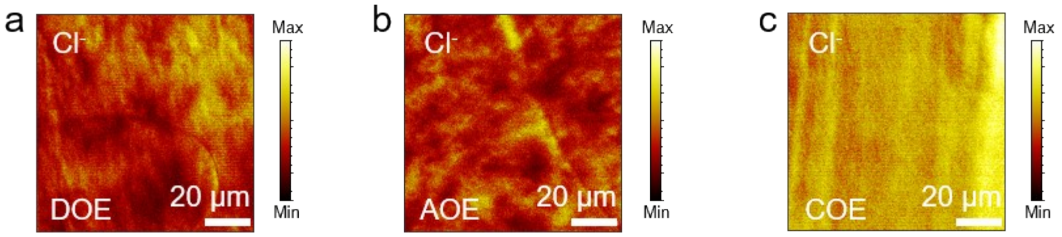

Figure S28. TOF-SIMS 2D depth distributions of Cl^- fragments in the SEI on Mg anodes cycled in (a) DOE, (b) AOE, and (c) COE after 20 cycles.

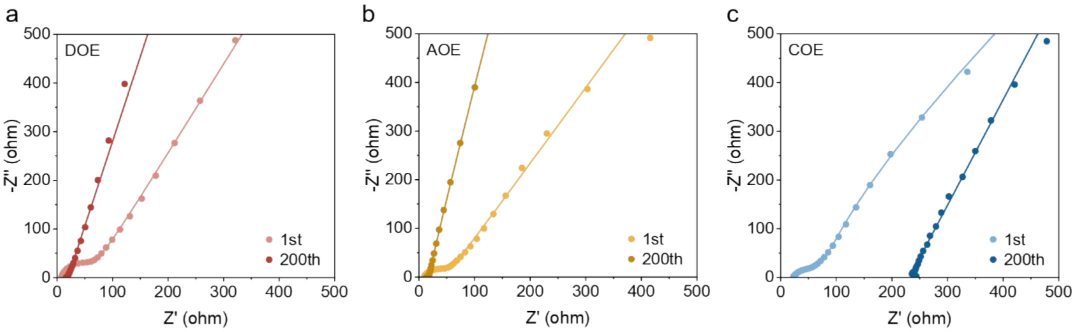

Figure S29. Nyquist plots of $Mg||Mo_6S_8$ cells using (a) DOE, (b) AOE, and (c) COE electrolytes, recorded after the 1st and 200th cycles.

The migration-barrier calculations suggest that MgF_2 presents a lower Mg^{2+} migration barrier than the more conventional MgO-type passivation product (Figure S27), indicating that a MgF_2-containing interphase may be more compatible with Mg^{2+} transport than a purely oxide-dominated blocking layer.

TOF-SIMS analysis of the SEI formed in DOE, AOE, and COE reveals a markedly stronger Cl^- signal in the near-surface region of the COE-derived interphase than in its DOE- and AOE-derived counterparts. This enrichment of chlorine-containing species points to more aggressive interfacial corrosion chemistry in COE, leading to a less stable SEI. In contrast, the MgF_2-rich interphase formed in DOE and AOE affords more effective protection of the Mg anode, consistent with their improved interfacial stability (Figure S28).

In addition, we performed EIS measurements after the first cycle and after 200 cycles. Even after 200 cycles, the DOE and AOE cells maintain well-defined semicircles, indicating that the interphases remain comparatively uniform and stable during long-term cycling. This behavior is consistent with the formation of a fluorine-containing, MgF_2-rich interphase that does not evolve into a highly heterogeneous or severely blocking layer. In contrast, the COE cell exhibits a dispersed and nonuniform impedance response rather than a well-defined semicircle, indicating pronounced interphase heterogeneity (Figure S29). These results further suggest that the interphase formed in DOE and AOE is fundamentally less passivating and more kinetically compatible than the interphase formed in COE.

In both AOE and DOE, $TFSI^-$ can contribute to the initial SEI formation on the anode through reductive decomposition. However, this does not imply that the resulting SEI is identical in the two systems. The decomposition pathway, extent of electrolyte consumption, and the stability of the resulting interphase are strongly affected by the coupled interfacial chemistry of the full cell. In the DOE system, besides the initial SEI formation from $TFSI^-$ on the anode, $PFTB^-$ undergoes limited oxidative decomposition at the cathode to form a protective CEI. Once this CEI is established, cathode-side parasitic reactions and cross-electrode interferences are significantly suppressed. This stabilizes the overall electrolyte environment and, in turn, allows the anode SEI to evolve in a more self-limiting and stable manner. By contrast, in AOE, although $TFSI^-$ is also present and can participate in SEI formation, the absence of a complementary cathode-side interphase leads to a less stable interfacial environment. As a result, the anode SEI is more susceptible to continuous perturbation from ongoing side reactions and cathode-derived species, leading to interphase characteristics that differ from those in DOE.

Supplementary Note 5. Interfacial conditioning in Mg||Mo_6S_8 cells.

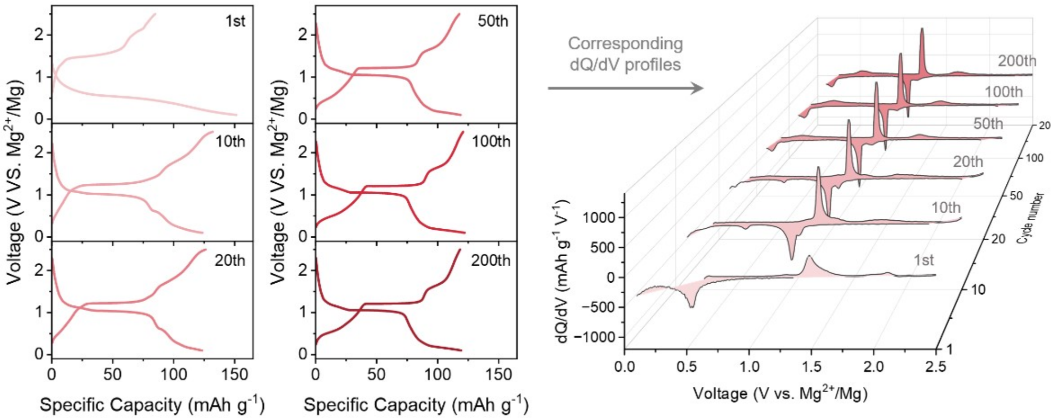

Figure S30. (a) Selected GCD curves (1st, 10th, 20th, 50th, 100th, and 200th cycles) of Mg||Mo_6S_8 cells operated at 1C in DOE electrolyte. (b) The corresponding differential capacity (d*Q*/d*V*) profiles.

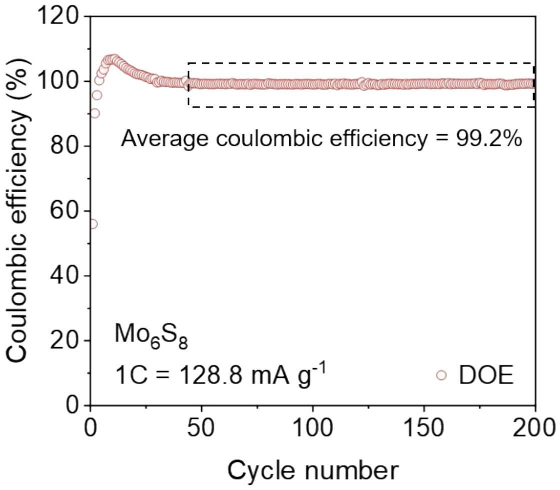

Figure S31. Coulombic efficiency of Mg||Mo_6S_8 cells operated at 1C in DOE.

It is worth noting that the electrochemical response of the Mg||Mo_6S_8 cells undergoes an initial conditioning stage during the early cycles. At this stage, the charge-discharge profiles show less well-defined plateaus, the corresponding d*Q*/d*V* features are broader and less symmetric (Figure S30), and the coulombic efficiency has not yet fully stabilized (Figure S31).

As cycling proceeds, the voltage profiles gradually converge to the characteristic plateaus of Mo_6S_8 redox chemistry, while the d*Q*/d*V* curves become well defined and highly reproducible (Figure S30). Together with the stabilization of the coulombic efficiency at a high level upon further cycling (Figure S31), these observations indicate that parasitic reactions become substantially suppressed after interfacial maturation, such that the subsequent electrochemical behavior is governed predominantly by reversible Mo_6S_8 redox processes. In our system, this stabilization is reached after approximately 50 cycles.

Supplementary Note 6. Analysis of cathode cross-talk.

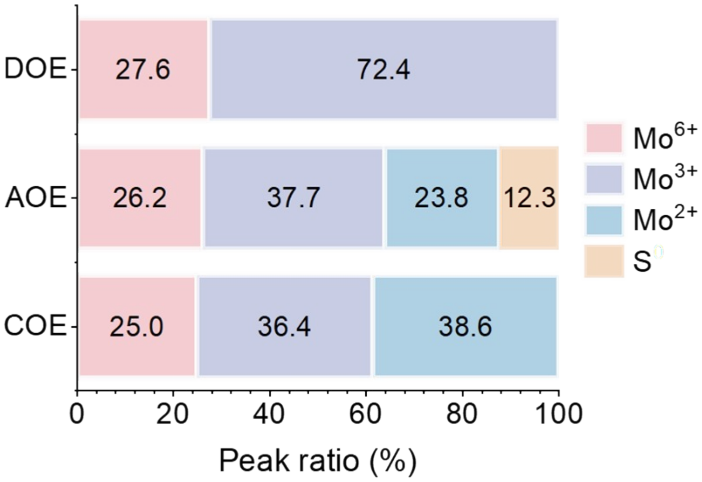

Figure S32. Proportions of Mo species in the anode for DOE, AOE, and COE, derived from statistical analysis of the XPS spectra shown in Figure S3b.

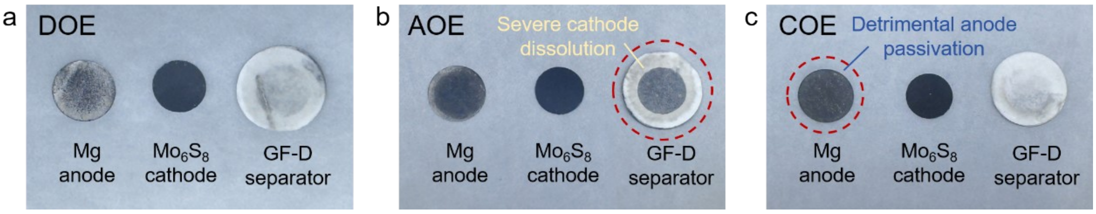

Figure S33. Optical images of the Mg anode, Mo_6S_8 cathode, and anode-side separator in DOE, AOE, and COE after 30 cycles.

In the AOE system, in addition to the Mo-related peaks, a distinct S 2s signal is observed on the anode. This indicates the migration of sulfur-containing species from the cathode, suggesting severe structural degradation and dissolution of Mo_6S_8. Meanwhile, the presence of multiple Mo oxidation states further supports the occurrence of significant dissolution and redeposition processes. In contrast, for the COE system, the S 2s signal is no longer detectable, indicating that the migration of sulfur species is effectively suppressed. However, a noticeable fraction of low-valence Mo^{2+} species is still present, implying that partial dissolution and subsequent deposition of Mo species still occur. More importantly, in the DOE system, only Mo^{6+} and Mo^{3+} species are observed, with no detectable Mo^{2+} or sulfur-related signals. This suggests that the dissolution of Mo_6S_8 is largely suppressed, and the redox process proceeds in a more controlled and reversible manner (Figure S32).

To more systematically compare the extent of cathode dissolution/cross-talk in different electrolytes, we performed post-mortem optical inspection of the Mg anode, the Mo_6S_8 cathode, and the separator facing the Mg side after 30 cycles in DOE, AOE, and COE. The results reveal clear differences among the three systems. In AOE, the separator on the Mg side became distinctly darker, and the Mg surface also showed obvious darkening, indicating the most severe migration of cathode-derived species to the anode side and thus the strongest cathode-to-anode cross-talk (Figure S33b). In

COE, the separator darkening was much weaker than in AOE, whereas the Mg surface still appeared substantially darkened. This suggests that, although the extent of transported species is lower than in AOE, the anode interphase in COE is less effectively protected and is more vulnerable to cross-talk-induced interfacial degradation (Figure S33c). In contrast, in DOE, the separator remained much lighter and the Mg surface retained an appearance closest to fresh metallic Mg, supporting that DOE most effectively suppresses cross-talk and stabilizes the Mg anode interface (Figure S33a).

Supplementary Note 7. Solvation structures of DOE, AOE, and COE.

Figure S34. Optical images of DME, DOE, AOE, and COE at room temperature.

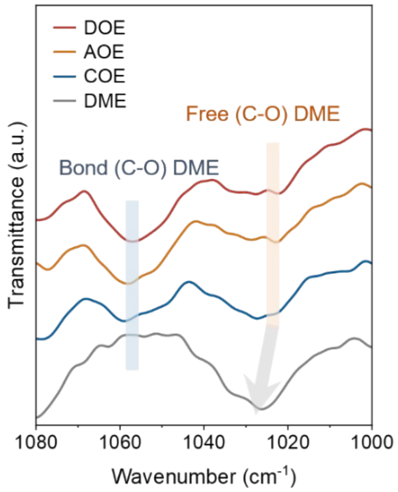

Figure S35. FTIR spectra of pure DME, DOE, AOE, and COE.

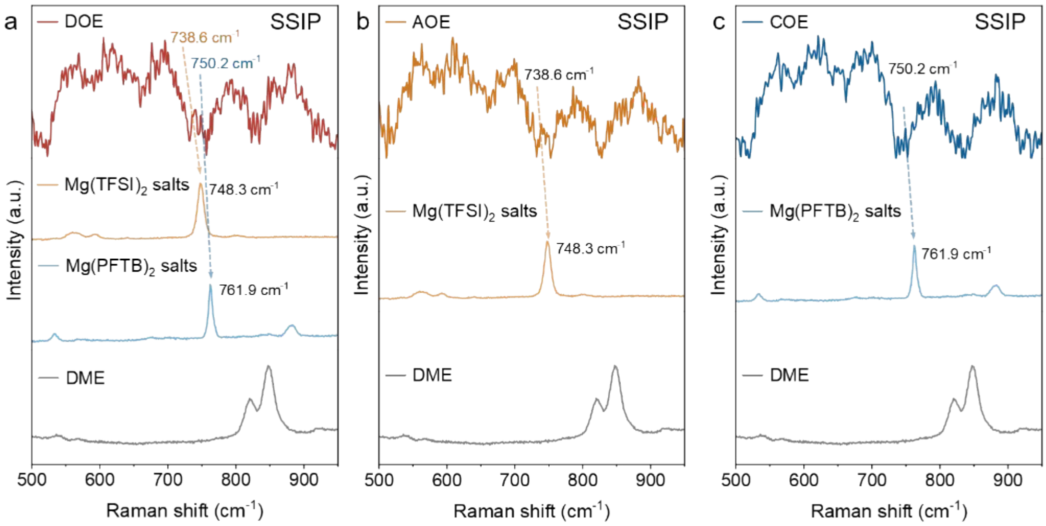

Figure S36. Raman spectra of pure DME, DOE, AOE, and COE, together with reference spectra of $Mg(TFSI)_2$ and $Mg(PFTB)_2$ salts.

As shown in Figure S34, the three electrolytes (DOE, AOE, and COE), together with the solvent DME, are all transparent, colorless, and homogeneous solutions, indicating no obvious macroscopic difference in appearance.

In the FTIR spectra, the characteristic DME C-O bands in all three electrolytes show an obvious blue shift compared with neat DME, indicating that Mg^{2+} strongly coordinates with DME and that solvent-coordinated structures are formed in all cases (Figure RS35).

In the Raman spectra, we further compared the characteristic vibrational bands of $Mg(TFSI)_2$ and $Mg(PFTB)_2$ solid salts with those of the corresponding DME-containing electrolytes. The characteristic peaks of the $Mg(TFSI)_2$ and $Mg(PFTB)_2$ solid salts are located at 748.3 and 761.9 cm^{-1}, respectively, which are typical signatures of contact ion pairs (CIPs). After the addition of DME, the CIP characteristic bands in all three electrolytes also shift noticeably, indicating that the coordination environment of the ions is significantly altered by solvation (Figure S36). These spectral features are consistent with solvation structures dominated by solvent-separated ion pairs (SSIPs), rather than by extensive ion aggregates (AGG). Therefore, the FTIR and Raman results suggest that AOE, COE, and DOE all share a similar solvent-coordinated and predominantly SSIP-type solvation environment. Under this premise, the distinct selective decomposition behavior is more reasonably attributed to the different intrinsic interfacial reactivities of $TFSI^-$ and $PFTB^-$ within a similar solvated environment, rather than to fundamentally different bulk solvation frameworks. In other words, the observed behavior arises from solvation-modulated interfacial chemistry, while the relative orbital/energy-level alignment serves as a qualitative guide to understand the preferential oxidation/reduction tendencies.

Supplementary Note 8. Electrolyte-replacement tests.

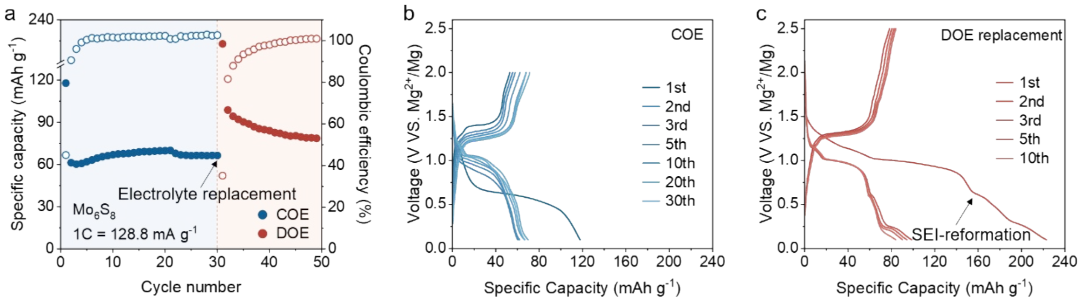

Figure S37. (a) Cycling performance of Mg||Mo_6S_8 cell at 1C in the COE electrolyte, and after electrolyte replacement with DOE. (b) GCD profiles at selected cycles in COE (1st, 2nd, 3rd, 5th, 10th, 20th, and 30th). (c) GCD profiles at selected cycles in DOE (1st, 2nd, 3rd, 5th, and 10th).

To clarify whether the superior performance of DOE originates primarily from the inherited interphases or from the immediate bulk-electrolyte environment, we performed an electrolyte-replacement experiment. Mg||Mo_6S_8 cells were first cycled in COE for 30 cycles to allow substantial interfacial evolution on both the Mg anode and the Mo_6S_8 cathode. The cells were then disassembled in an Ar-filled glovebox, and the harvested electrodes were reassembled into fresh cells using DOE as the electrolyte under otherwise identical testing conditions (Figure S37a).

A pronounced extra discharge process was observed in the first cycle after electrolyte replacement (Figure S37c). This feature is primarily attributed to re-establishment of a DOE-compatible SEI on the Mg anode, together with partial re-equilibration of the inherited interphases upon switching from COE to DOE. After this initial adjustment stage, the reassembled cells exhibited clearly improved cycling behavior relative to the original COE cells, together with recovery of the wider operating voltage window characteristic of DOE.

These observations indicate that the subsequent electrochemical behavior is strongly influenced by the inherited dual interphases and their re-equilibration upon electrolyte replacement, rather than being determined solely by the immediate bulk-electrolyte environment. In this sense, the advantage of DOE lies in its ability to establish a mutually stabilizing SEI/CEI pair that suppresses interfacial parasitic reactions and enables more stable cycling.

Supplementary Note 9. Electrochemical behavior of the MACC baseline electrolyte.

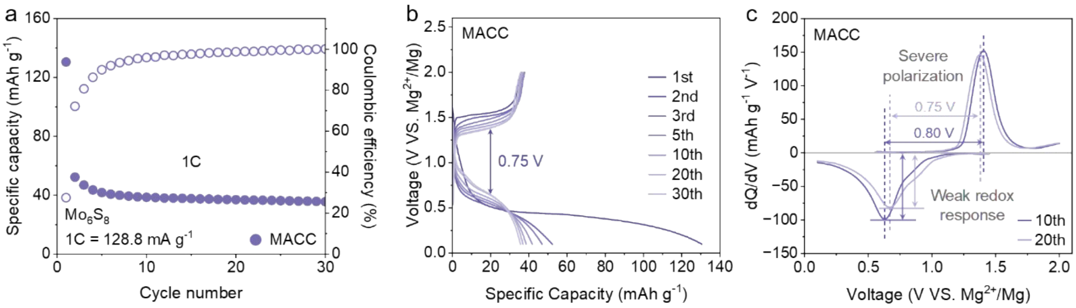

Figure S38. (a) Cycling performance of Mg||Mo_6S_8 cell at 1C in the MACC electrolyte. (b) GCD profiles at selected cycles in the MACC electrolyte (1st, 2nd, 3rd, 5th, 10th, 20th, and 30th). (c) d*Q*/d*V* profiles at the 10th and 20th cycles.

To provide a full-cell baseline, the Mg||Mo_6S_8 full-cell using the pristine MACC electrolyte was also evaluated. The GCD profiles exhibit an anomalously high discharge capacity in the first cycle, suggesting pronounced parasitic side reactions, likely arising from electrolyte decomposition. In the following cycles, the capacity rapidly decays to ~37 mAh g^{-1}, indicating that the pristine MACC electrolyte fails to provide sufficient interfacial stabilization for reversible full-cell operation (Figure S38b). Consistently, the corresponding d*Q*/d*V* curves display the characteristic redox peaks of Mo_6S_8, but with a large polarization of ~0.75 V, reflecting sluggish reaction kinetics and unstable electrode-electrolyte interphases in the absence of additives (Figure S38c).

Supplementary Table 1. Comparison of this work with state-of-the-art Mg||Mo_6S_8 cells.

Specific Current (mA/g)	Cycle number	Specific Capacity (mAh/g)	Refs
128.8	200 1000	119.3 97.2	This work
25.6	200	70	Joule 7.12 (2023): 2798-2813
1.288	5	38	J. Am. Chem. Soc. 2016, 138, 28, 8682-8685
12.88	50	78	Energy Environ. Sci. 5.10 (2012): 9100-9106.
128.8	800	60	Adv. Mater. 34.30 (2022): 2203783
64.4	250	72	Adv. Mater. 31.11, (2019): 1805930
100	500	43.9	Angew. Chem. Int. Ed. 64.5 (2025): e202417450.
64.4 128.8	200 500	72.1 64.4	Angew. Chem. Int. Ed. 62.21 (2023): e202301934.
20	50	45	Angew. Chem. Int. Ed. 61.30 (2022): e202205187.
25.6	100	92	Angew. Chem. Int. Ed. 131.23 (2019): 7697-7701.

10	10	80	Angew. Chem. Int. Ed. 127.27 (2015): 8011-8015.
100	120	47	Angew. Chem. Int. Ed. 126.12 (2014): 3237-3241.
128.8	40	44	Angew. Chem. Int. Ed. 51.39 (2012): 9780
100	100	70	ACS Energy Letters 8.1 (2022): 780-789.
6.4	210	57	ACS Energy Letters 6.9 (2021): 3212-3220.
2.56	100	49	

References

1. Yang, Y., Wang, J., Du, X., Jiang, H., Du, A., Ge, X., Li, N., Wang, H., Zhang, Y., Chen, Z., et al. Cation Co-Intercalation with Anions: The Origin of Low Capacities of Graphite Cathodes in Multivalent Electrolytes. J. Am. Chem. Soc. (2023) *145*, 12093–12104. https://doi.org/10.1021/jacs.3c01555.
2. Watkins, T., Kumar, A., and Buttry, D.A. Designer Ionic Liquids for Reversible Electrochemical Deposition/Dissolution of Magnesium. J. Am. Chem. Soc. (2016) *138*, 641–650. https://doi.org/10.1021/jacs.5b11031.
3. Wang, S., Wang, K., Zhang, Y., Jie, Y., Li, X., Pan, Y., Gao, X., Nian, Q., Cao, R., Li, Q., et al. High-entropy Electrolyte Enables High Reversibility and Long Lifespan for Magnesium Metal Anodes. Angew Chem Int Ed (2023) *62*, e202304411. https://doi.org/10.1002/anie.202304411.
4. Xiao, J., Zhang, X., Fan, H., Zhao, Y., Su, Y., Liu, H., Li, X., Su, Y., Yuan, H., Pan, T., et al. Stable Solid Electrolyte Interphase In Situ Formed on Magnesium-Metal Anode by using a Perfluorinated Alkoxide-Based All-Magnesium Salt Electrolyte. Advanced Materials (2022) *34*. https://doi.org/10.1002/adma.202203783.
5. Ding, P., Yuan, H., Xu, L., Wu, L., Du, H., Zhao, S., Yu, D., Qin, Z., Liu, H., Li, Y., et al. Coordination Regulation Enabling Deep Eutectic Electrolyte for Fast-Charging High-Voltage Lithium Metal Batteries. Advanced Materials (2025) *37*, 2413654. https://doi.org/10.1002/adma.202413654.
6. Wang, E., Jónsson, E., and Grey, C.P. NMR Methodology for Measuring Dissolved O_2 and Transport in Lithium–Air Batteries. J. Phys. Chem. C (2023) *127*, 10001–10011. https://doi.org/10.1021/acs.jpcc.3c00991.
7. Yuan, Z., Han, B., Liu, B., Sun, J., Zhou, P., Mu, R., and Zhang, Z. Unexpected activity of MgO nanoclusters for the reductive-coupling synthesis of organonitrogen chemicals with C = N bonds. Nat Commun (2025) *16*, 2963. https://doi.org/10.1038/s41467-025-58222-6.
8. Hou, S., Ji, X., Gaskell, K., Wang, P., Wang, L., Xu, J., Sun, R., Borodin, O., and Wang, C. Solvation sheath reorganization enables divalent metal batteries with fast interfacial charge transfer kinetics. Science (2021) *374*, 172–178. https://doi.org/10.1126/science.abg3954.
9. Tan, J., Feng, L., Shao, J., Zhang, W., Qin, H., Liu, H., Shu, Y., Yang, L., Meng, Y., Tang, Y., et al. *In Situ* Li^+ Intercalation into Nanosized Chevrel Phase Mo_6 S_8 toward Efficient Electrochemical Nitroarene Reduction. J. Am. Chem. Soc. (2025) *147*, 10118–10128. https://doi.org/10.1021/jacs.4c14111.
10. Li, C., Shyamsunder, A., Key, B., Yu, Z., and Nazar, L.F. Stabilizing magnesium plating by a low-cost inorganic surface membrane for high-voltage and high-power Mg batteries. Joule (2023) *7*, 2798–2813. https://doi.org/10.1016/j.joule.2023.10.012.
11. Liu, Y., Tao, X., Wang, Y., Jiang, C., Ma, C., Sheng, O., Lu, G., and Lou, X.W. (David) Self-assembled monolayers direct a LiF-rich interphase toward long-life lithium metal batteries. Science (2022) *375*, 739–745. https://doi.org/10.1126/science.abn1818.
12. Li, C., Guha, R.D., Shyamsunder, A., Persson, K.A., and Nazar, L.F. A weakly ion pairing electrolyte designed for high voltage magnesium batteries. Energy Environ. Sci. (2024) *17*, 190–201. https://doi.org/10.1039/D3EE02861E.
13. Zhou, J., Wu, F., Mei, Y., Hao, Y., Li, L., Xie, M., and Chen, R. Establishing Thermal Infusion Method for Stable Zinc Metal Anodes in Aqueous Zinc-Ion Batteries. Advanced Materials (2022) *34*, 2200782. https://doi.org/10.1002/adma.202200782.

14. Kim, H.S., Arthur, T.S., Allred, G.D., Zajicek, J., Newman, J.G., Rodnyansky, A.E., Oliver, A.G., Boggess, W.C., and Muldoon, J. Structure and compatibility of a magnesium electrolyte with a sulphur cathode. Nat Commun (2011) *2*, 427. https://doi.org/10.1038/ncomms1435.